

## The $\beta$ Pictoris b Hill sphere transit campaign

### II. Searching for the signatures of the $\beta$ Pictoris exoplanets through time delay analysis of the $\delta$ Scuti pulsations

Sebastian Zieba<sup>1,2,3</sup>, Konstanze Zwintz<sup>3</sup>, Matthew Kenworthy<sup>2</sup>, Daniel Hey<sup>4</sup>, Simon J. Murphy<sup>5</sup>,  
Rainer Kuschnig<sup>6</sup>, Lyu Abe<sup>7</sup>, Abdelkrim Agabi<sup>7</sup>, Djamel Mekarnia<sup>7</sup>, Tristan Guillot<sup>7</sup>,  
Fran ois-Xavier Schmider<sup>7</sup>, Philippe Stee<sup>7</sup>, Yuri De Pra<sup>8</sup>, Marco Buttu<sup>9,10</sup>, Nicolas Crouzet<sup>2</sup>,  
Samuel Mellon<sup>11</sup>, Jeb Bailey III<sup>12</sup>, Remko Stuik<sup>2</sup>, Patrick Dorval<sup>13</sup>, Geert Jan Talens<sup>14</sup>, Steven Crawford<sup>15,19</sup>,  
Eric Mamajek<sup>11,16</sup>, Iva Laginja<sup>17</sup>, Michael Ireland<sup>18</sup>, Blaine Lomberg<sup>19,20</sup>, Rudi Kuhn<sup>19</sup>, Ignas Snellen<sup>2</sup>,  
Paul Kalas<sup>22,23,24</sup>, Jason J. Wang<sup>25</sup>, Kevin B. Stevenson<sup>26</sup>, Ernst de Mooij<sup>27,28</sup>,  
Anne-Marie Lagrange<sup>17,29</sup>, Sylvestre Lacour<sup>17,30</sup>, Mathias Nowak<sup>31</sup>, Paul A. Str m<sup>32,33</sup>,  
Zhang Hui<sup>34</sup>, and Lifan Wang<sup>35</sup>

(Affiliations can be found after the references)

Received 18 August 2023 / Accepted 12 March 2024

#### ABSTRACT

The  $\beta$  Pictoris system is the closest known stellar system with directly detected gas giant planets, an edge-on circumstellar disc, and evidence of falling sublimating bodies and transiting exocomets. The inner planet,  $\beta$  Pictoris c, has also been indirectly detected with radial velocity (RV) measurements. The star is a known  $\delta$  Scuti pulsator, and the long-term stability of these pulsations opens up the possibility of indirectly detecting the gas giant planets through time delays of the pulsations due to a varying light travel time. We search for phase shifts in the  $\delta$  Scuti pulsations consistent with the known planets  $\beta$  Pictoris b and c and carry out an analysis of the stellar pulsations of  $\beta$  Pictoris over a multi-year timescale. We used photometric data collected by the BRITE-Constellation, bRing, ASTEP, and TESS to derive a list of the strongest and most significant  $\delta$  Scuti pulsations. We carried out an analysis with the open-source python package `maelstrom` to study the stability of the pulsation modes of  $\beta$  Pictoris in order to determine the long-term trends in the observed pulsations. We did not detect the expected signal for  $\beta$  Pictoris b or  $\beta$  Pictoris c. The expected time delay is 6 s for  $\beta$  Pictoris c and 24 s for  $\beta$  Pictoris b. With simulations, we determined that the photometric noise in all the combined data sets cannot reach the sensitivity needed to detect the expected timing drifts. An analysis of the pulsational modes of  $\beta$  Pictoris using `maelstrom` showed that the modes themselves drift on the timescale of a year, fundamentally limiting our ability to detect exoplanets around  $\beta$  Pictoris via pulsation timing.

**Key words.** asteroseismology – methods: observational – techniques: photometric – planets and satellites: general – stars: individual:  $\beta$  pictoris – stars: variables:  $\delta$  Scuti

#### 1. Introduction

$\beta$  Pictoris is a nearby southern hemisphere star visible with the naked eye for which  $\delta$  Scuti-like pulsations were discovered by Koen (2003). The planetary-mass companion  $\beta$  Pictoris b was detected using the VLT/NaCo instrument with direct imaging (Lagrange et al. 2009b, 2010). Evidence of a second planet in the  $\beta$  Pictoris system was published by Lagrange et al. (2019b) using the radial velocity (RV) method and recently independently confirmed by Nowak et al. (2020) and Lagrange et al. (2020) using VLTI/GRAVITY observations.

The lifetime and frequency stability of  $\delta$  Scuti pulsations make them astronomical “stellar clocks,” and therefore, they are great targets for applying timing techniques (Compton et al. 2016). The common orbital motion of a star together with a companion around the barycenter of a system results in a periodic early or late arrival of the stellar pulsational signals. This principle led to the first detection of planets orbiting a pulsar outside the Solar System (Wolszczan & Frail 1992; Wolszczan 1994). The periodic variation of the arrival times can be seen as

either a frequency modulation (FM; Shibahashi & Kurtz 2012; Shibahashi et al. 2015) or a phase modulation (PM; Murphy et al. 2014; Murphy & Shibahashi 2015; Murphy et al. 2016b). The latter perspective works better for companions in wider orbits.

By applying the PM method on Kepler data, Murphy et al. (2016a) discovered a massive planet ( $m \sin i \approx 12 M_J$ ) with an orbital period of about 840 days around a  $\delta$  Scuti star. In addition to the discovery of this planet, the PM method has led to the detection of 341 binaries and hundreds of more candidates (Murphy et al. 2018). Furthermore, it has provided us with the eccentricity, period, and mass function of these companions orbiting stars, just as the RV method does (e.g. Nesvold & Kuchner 2015). Applying the same method to pulsating stars observed by the TESS mission will lead to many more binary systems with full orbital solutions.

In this work, we use the data collected by the TESS satellite in its primary mission and data collected by the Hill sphere<sup>1</sup> transit campaign, which was an international effort of space-based

<sup>1</sup> The Hill sphere is the region around a planet where masses, such as moons and planetary rings, are gravitationally bound to the planet.

(e.g. through the BRITE-Constellation) and ground-based (e.g. through bRing, ASTEP) observations that searched for signatures of material around the giant planet  $\beta$  Pictoris b (Kalas et al. 2019; Kenworthy 2017). We analyzed this photometric data by searching for phase variations (and therefore time delays) caused by orbital motion in the pulsational signals.  $\beta$  Pictoris was observed for approximately four months from October 2018 to February 2019 during the primary mission of TESS. A second visit occurred during TESS' extended mission from November 2020 to February 2021.

In Sect. 2, we describe the properties of the different components in the  $\beta$  Pictoris system. Section 3 has a summary of all observational instruments and a frequency analysis for the photometry collected by TESS. The theory and equations for this paper can be found in Sect. 4, and our results and conclusions follow in Sects. 5 and 6.

## 2. The $\beta$ Pictoris system

$\beta$  Pictoris (HD 39060; HR 2020) is one of the most studied and intriguing star-planet systems. The Infrared Astronomical Satellite (IRAS) discovered an infrared excess (Aumann et al. 1984) for this bright and close southern star that was attributed to the presence of a circumstellar disc. This disc was first imaged by Smith & Terrile (1984) and clearly showed the edge-on geometry of this system. The gas and dust in this disc is mostly “second generation,” that is, constantly replenished by collisions of comets and asteroids (Lagrange et al. 2020). A warp in this disc (Augereau et al. 2001; Mouillet et al. 1997; Nesvold & Kuchner 2015) and signatures of evaporating exocomets (also called falling evaporating bodies, or FEBs) in spectroscopy (Ferlet et al. 1987; Beust & Morbidelli 2000) were attributed to an exoplanet orbiting the star interacting dynamically with its environment (for more information on exocomets observed around  $\beta$  Pictoris detected in photometry, see Zieba et al. 2019; Strøm et al. 2020; Pavlenko et al. 2022; Lecavelier des Etangs et al. 2022).

### 2.1. The star

Koen (2003) discovered  $\delta$  Scuti-type pulsations at the millimagnitude level originating from  $\beta$  Pictoris. Further analysis by Mékarnia et al. (2017), Zwintz et al. (2019), and Zieba et al. (2019) showed dozens of additional frequencies between 20 and 80 cycles per day. An asteroseismic large spacing,  $\Delta\nu$ , has been measured for  $\beta$  Pictoris (Bedding et al. 2020), which might facilitate a precise asteroseismic age in the future. The pulsations also induce intrinsic variations in the RV at  $\lesssim 1$  km s $^{-1}$  peak to peak (Lagrange et al. 2009a, 2012; Galland et al. 2006), which hampers the search for planets with the RV method in this system. A selection of the fundamental properties of the star  $\beta$  Pictoris are listed in Table 1.

### 2.2. The planets: $\beta$ Pictoris b and c

The warp of the inner disc of  $\beta$  Pictoris observed by the *Hubble* Space Telescope and in ground-based observations was one of the indirect lines of evidence for a massive substellar companion orbiting the star (Burrows et al. 1995; Mouillet et al. 1997; Heap et al. 2000; Golimowski et al. 2006). Signatures of infalling exocomets in the spectra of the star also needed a “perturber” to scatter them onto eccentric inner system-bearing orbits. The planet,  $\beta$  Pictoris b, was then discovered using the VLT/NaCo instrument data in 2003 (Lagrange et al. 2009b) and was later confirmed by Lagrange et al. (2010). A transit-like

**Table 1.** Various stellar parameters of the star  $\beta$  Pictoris.

Parameter	Value	Reference
RA (J2000.0)	05 h 47 m 17.09 s	1
Dec (J2000.0)	-51 h 03 m 59.41 s	1
$V$ (mag)	3.86	2
TESS (mag)	3.696	1
Age (Myr)	$23 \pm 3$	3
Parallax (mas)	$50.93 \pm 0.15$	4, 5, 6
Distance (pc)	$19.63 \pm 0.06$	4, 5, 6
Spectral class	A6V	7
Radius ( $R_\odot$ )	$1.497 \pm 0.025$	8
Mass ( $M_\odot$ )	$1.75^{+0.03}_{-0.02}$	9
Teff (K)	$8090 \pm 59$	8

**References.** (1) Stassun et al. (2019); (2) Cousins (1971); (3) Mamajek & Bell (2014); (4) Gaia Collaboration (2016); (5) Gaia Collaboration (2023); (6) Lindegren et al. (2021); (7) Gray et al. (2006); (8) Zwintz et al. (2019); (9) Lacour et al. (2021).

**Table 2.** Various parameters of the planets  $\beta$  Pictoris b and c based on Lacour et al. (2021).

Parameter	Unit	$\beta$ Pictoris b	$\beta$ Pictoris c
Mass	$M_J$	$11.90^{+2.93}_{-3.04}$	$8.89^{+0.75}_{-0.75}$
$a$	au	$9.93^{+0.03}_{-0.03}$	$2.68^{+0.02}_{-0.02}$
$e$	—	$0.103^{+0.003}_{-0.003}$	$0.32^{+0.02}_{-0.02}$
$i$	°	$89.00^{+0.00}_{-0.01}$	$88.95^{+0.09}_{-0.10}$
$\varpi^{(a)}$	°	$199.3^{+2.8}_{-3.1}$	$66.0^{+1.8}_{-1.7}$
$\tau^{(b)}$	—	$0.719^{+0.008}_{-0.010}$	$0.724^{+0.006}_{-0.006}$
$P$	yr	$23.61^{+0.09}_{-0.09}$	$3.34 \pm 0.04$
$P$	days	$8623^{+31}_{-32}$	$1221 \pm 15$
$t_p^{(c)}$	MJD	65243	59888

**Notes.** <sup>(a)</sup>The argument of periastron  $\varpi$  reported in Lacour et al. (2021) follows the definition in Blunt et al. (2020) and therefore refers to the orbit of the companion and not to the star. In this paper, however, we refer to the orbit of the star when we use  $\varpi$ . <sup>(b)</sup>Reference epoch MJD 59000 (31 May 2020). <sup>(c)</sup>Derived from  $\tau$ .

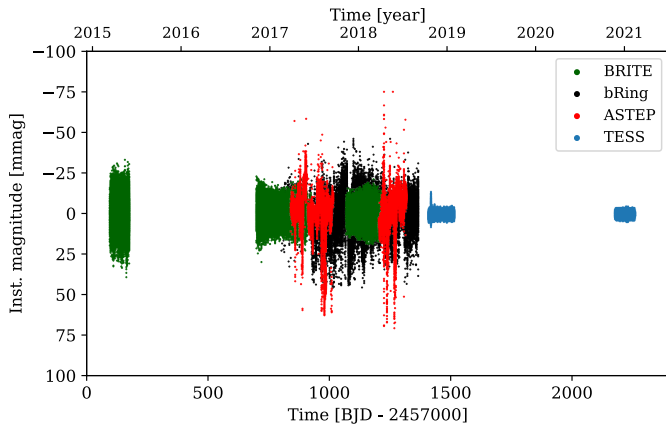
event was observed in 1981 and attributed to a planet (Lecavelier Des Etangs et al. 1995). However, a better orbit determination with the VLT/SPHERE instrument ruled out  $\beta$  Pictoris b as the cause of that event (Lagrange et al. 2019a). Using data from the Gemini Planet Imager, Wang et al. (2016) were able to rule out a transit of the planet  $\beta$  Pictoris b during the conjunction in 2017 at a  $10\sigma$  level. However, a Hill sphere transit was predicted for the time between late 2017 and early 2018 (Lecavelier des Etangs & Vidal-Madjar 2016; Wang et al. 2016). Various observational campaigns were initiated by PicSat (Nowak et al. 2018; Menegaldo et al. 2022); bRing (Kenworthy 2017); and the BRITE-Constellation (Weiss et al. 2014) in order to photometrically observe possible material around the planet; however, there was no significant detection (Kenworthy et al. 2021). The mass and the orbital solution of the outer planet  $\beta$  Pictoris b are listed in Table 2.

Evidence of an additional planet in the  $\beta$  Pictoris system was published by Lagrange et al. (2019b). Over 6000 spectra of the star taken between 2003 and 2018 by the HARPS instrument at the ESO La Silla 3.6 m telescope have been analyzed,

**Table 3.** Summary of the properties of the various instruments and corresponding light curves.

Observation	Wavelength (nm)	Observation start	Observation end	$T$ (days)	$1/T$ ( $10^{-3}$ day $^{-1}$ )	$f_{Ny.}$ (day $^{-1}$ )	cadence (s)	DC (%)
BHr	550–700	16 March 2015	2 June 2015	78.32	12.77	4167	10.37	6.78
BTr + BHr	550–700	4 Nov. 2016	17 June 2017	224.6	4.453	2128	20.30	7.07
BHr	550–700	9 Nov. 2017	25 April 2018	167.3	5.976	2128	20.30	7.48
bRing	463–639	2 Feb. 2017	1 Sept. 2018	575.5	1.738	135.4	319.1	27.0
ASTEP17	695–844	28 March 2017	14 Sept. 2017	170.0	5.881	495.8	87.13	18.9
ASTEP18	695–844	28 March 2018	15 July 2018	109.3	9.150	502.8	85.92	29.2
TESS	600–1000	19 Oct. 2018	1 Feb. 2019	105.2	9.507	360.0	120.0	85.3
TESS	600–1000	20 Nov. 2020	8 Feb. 2021	79.8	12.53	360.0	120.0	90.2

**Notes.** The term  $T$  denotes the time base of the observations, the reciprocal value  $1/T$  corresponds to the Rayleigh criterion,  $f_{Ny.}$  is the Nyquist frequency, and DC is the duty cycle. BRITE Lem (BLb) is equipped with a blue filter and observed  $\beta$  Pictoris from December 2016 until June 2017, but due to significantly higher noise in the time series, the data was disregarded from the analysis. See [Zwintz et al. \(2019\)](#) for an analysis of the BLb observations.

**Fig. 1.** Full light curve of all available observations of the star  $\beta$  Pictoris used in this work.

and they showed a hint of a planetary signal.  $\beta$  Pictoris c was then ultimately directly detected by [Nowak et al. \(2020\)](#) and [Lagrange et al. \(2020\)](#) using VLTI/GRAVITY observations. A list of parameters for the planet can be found in Table 2.

### 3. Observations

Due to the 2017–2018 Hill Sphere Transit of  $\beta$  Pictoris b, an international campaign of space- and ground-based observations was launched in order to search for signatures of material around the giant planet ([Kalas et al. 2019](#); [Kenworthy et al. 2021](#)). Table 3 summarizes various properties of the different light curves and Fig. 1 shows the full light curve. Changes to those light curves other than the Gaussian high-pass procedure, which is explained in Appendix A.2, are noted in the following subsections. The data provided by BRITE-Constellation was left unchanged. A detailed analysis of the photometry of  $\beta$  Pictoris collected by BRITE-Constellation and bRing was published by [Zwintz et al. \(2019\)](#). As we wanted to measure the periodic motion of a star around a barycenter, we also wanted to correct for the motion of the Earth in the Solar System. All the observations in this work were therefore converted to the Barycentric Julian Date in the barycentric dynamical time (BJD<sub>TBD</sub>) standard using the Python tool BARYCORRPy ([Kanodia & Wright 2018](#)), which is based on the IDL code BARYCORR ([Wright & Eastman 2014](#)).

#### 3.1. BRITE-Constellation

The BRITE-Constellation ([Weiss et al. 2014](#)) consists of five nanosatellites collecting photometry for the brightest stars on the sky. In this work, we analyzed data collected by three of the satellites: BRITE-Heweliusz (BHr), BRITE-Toronto (BTr), and BRITE-Lem (BLb). Being in a low-earth orbit, the orbital periods of the satellites are all around 100 min. A minimum of 15 min per orbit is dedicated to observations. Three different runs were conducted in the constellations around Pictor and Vela, which also included the star  $\beta$  Pictoris. A summary of the durations and various properties of the observations can be found in Table 3. The pipeline for the photometry reduction is described in [Popowicz et al. \(2017\)](#). An analysis of all BRITE observations was conducted in [Zwintz et al. \(2019\)](#). For the three runs by BHr, BTr+BHr, and BHr, which all used the red BRITE filter, six, 13, and eight significant frequencies were extracted, respectively. The only run with a blue filter by BLb suffered from higher noise compared to the other BRITE observations. [Zwintz et al. \(2019\)](#) has reported four frequencies in the collected BLb photometry. The blue observations were discarded from this analysis, as the data quality was not good enough to provide additional information.

#### 3.2. bRing

The bRing project (which stands for “the  $\beta$  Pictoris b Ring project”) was initiated in order to collect photometry of  $\beta$  Pictoris during the Hill sphere transit of  $\beta$  Pictoris b at the end of 2017 ([Stuik et al. 2017](#)). To that end, two stations in South Africa and Australia were built, each consisting of two wide-field cameras. Their design is based on the Multi-Site All-Sky CAmeRA (MASCARA; [Snellen et al. 2012](#); [Talens et al. 2017](#)). The capability of bRing to monitor bright stars and find previously unknown variables has been shown by [Mellon et al. \(2019\)](#). More information on the observing strategy and design of bRing can be found in [Stuik et al. \(2017\)](#). The reduction pipeline for the MASCARA and bRing instruments is described in [Talens et al. \(2018\)](#). With a passband of 463–639 nm, bRing collected the shortest wavelengths of all observatories considered in this work. We expected to see the highest pulsational amplitudes in these data, as  $\beta$  Pictoris is a star of spectral type A6 ([Zwintz et al. 2019](#)) and has its energy maximum in the blue optical wavelengths. Due to some evident outliers in the data, one  $5\sigma$

clip with respect to the median of the data set was applied. This significantly weakened the one-day aliases in the spectral window. An iterative sigma clipping procedure was not conducted due to noticeable changes in the amplitudes of the pulsations in this case (see Hogg et al. 2010 for a discussion of sigma clipping in order to remove outliers). The observations by bRing were separated into two equally sized segments in order to gain more time delay measurements while also maintaining a precision in frequency and phase comparable to the ASTEP observations. Zwintz et al. (2019) found six significant frequencies in the photometry collected by bRing. All of them are also identified in the data collected by BRITE, ASTEP, and TESS.

### 3.3. ASTEP

The Antarctic Search for Transiting ExoPlanets, or ASTEP, is an automated telescope with an aperture of 40 cm located at the Concordia station at Dome C in Antarctica (Abe et al. 2013; Guillot et al. 2015; Mékarnia et al. 2017). It uses a Sloan  $i'$  filter (centered at 763 nm). We only used measurements with a sun elevation lower than  $-18^\circ$ . Notably, data points where the centroid of the star did not fall on the central pixel suffer from strong outliers. The removal of these outliers and a  $5\sigma$  clip with respect to the median weakened aliases significantly but without noticeable changes in the amplitude of the strongest pulsational frequencies. Mékarnia et al. (2017) conducted a frequency analysis of the  $\beta$  Pictoris photometry collected by the ASTEP observatory, and they are consistent with the ones seen in the TESS data.

### 3.4. TESS

The Transiting Exoplanet Survey Satellite (TESS; Ricker et al. 2015) was launched in April 2018 in order to find transiting exoplanets around nearby bright stars. The data of  $\beta$  Pictoris (TIC 270577175,  $T = 3.696$  mag) was collected from 19 October 2018 to 1 February 2019 in sectors four through seven and from 20 November 2020 to 8 February 2021 in the sectors 32 through 34. The data for first four sectors were obtained during TESS' primary mission, and data for the three other sectors were obtained approximately 2 yr later as part of the first extended mission.  $\beta$  Pictoris is one of the preselected targets for which short-cadence (2 min) data are provided. Due to the high-cadence data, the high photometric precision of TESS, its high duty cycle, and the long baseline,  $\delta$  Scuti pulsations can be resolved and identified with high precision. The photometric data of  $\beta$  Pictoris as observed by TESS was accessed and modified with the Python package `Lightkurve` (Lightkurve Collaboration 2018), which retrieves the data from the MAST archive<sup>2</sup>. For this analysis, we used the Pre-search Data Conditioning Simple Aperture Photometry (PDCSAP; Smith et al. 2012; Stumpe et al. 2012) light curves, which are produced from the Science Processing Operations Center (SPOC) pipeline (Jenkins et al. 2016, 2010; Jenkins 2017). These PDCSAP light curves were corrected for systematics by the SPOC pipeline. We also visually inspected the target pixel files (TPF) in order to rule out various instrumental and astrophysical effects, such as Solar System asteroids or comets crossing the field of view. A comparison of the Lomb–Scargle periodogram (Lomb 1976; Scargle 1982) of the raw simple aperture photometry and PDCSAP light curves showed a significant change in the noise at low frequencies. This is due to the systematic effects present in sector four. The lowest noise in the low-frequency range can be found for the PDCSAP light curve

with a completely removed fourth sector. This light curve was then used for the main frequency analysis.

The individual sectors were normalized by dividing each of the sectors by their respective median flux, and the sectors were combined into one light curve. Furthermore, every measurement with a non-zero quality flag (see Sect. 9 in the TESS Science Data Products Description Document)<sup>3</sup> was removed. Such anomalies as cosmic ray events or instrumental issues were marked by these quality flags.

The frequency analysis was conducted using the Python package `SMURFS` (Müller 2020) and checked with the software package `Period04` (Lenz & Breger 2005). Following Breger et al. (1993), all pulsation frequencies down to a signal-to-noise ratio of four were extracted. The frequency range analyzed is between zero and the Nyquist frequency of 360 cycles per day. Following the procedure described in Zieba et al. (2019), 37 significant p-modes in frequencies ranging from 34 to  $76\text{ day}^{-1}$  were identified. As we are only interested in the strongest pulsational frequencies for this time delay analysis, we did not try to further recover any of the lower amplitude modes. A list of the extracted frequencies can be found in Table A.1.

## 4. Theory and methodology

In this chapter, we discuss the theory behind time delays and the methods used in order to finally arrive at the time delay plot. Importantly, this plot can be used to search for companions around pulsating stars.

### 4.1. $\delta$ Scuti stars

$\delta$  Scuti stars can be found at the intersection region between the main sequence and the instability strip on the Hertzsprung–Russel diagram. Thanks to the nearly uninterrupted, high-precision photometry of Kepler's primary 4-yr mission, the general understanding of pulsating stars has been revolutionized.  $\delta$  Scuti stars have masses between approximately 1.5 and  $2.5 M_\odot$ . They pulsate in radial and non-radial low-degree, low-order pressure ( $p$ ) modes that are primarily driven by an opacity mechanism (also called a  $\kappa$ -mechanism) in their HeII zone with contributions from turbulent pressure (Houdek 2000; Antoci et al. 2014) and the edge-bump mechanism (Murphy et al. 2020b). The oscillations have periods between 18 min and 8 h respectively 80 and three cycles per day (Aerts et al. 2010). Linear combinations of those oscillations can, however, create peaks at lower frequencies (Breger & Montgomery 2014). Besides main-sequence and more-evolved stars,  $\delta$  Scuti pulsations were observed in pre-main-sequence stars, thus giving us the possibility to learn about early stellar evolution (Zwintz et al. 2014; Murphy et al. 2021; Steindl et al. 2022).

### 4.2. The ephemeris equation

The search for time delays in certain astrophysical signals requires a (quasi-)periodic process in space. A review on this and the related equations can be found in Hermes (2018). There are different processes that are “clock-like” under the assumption of a closed system, including the exceptionally stable signals of pulsars, the eclipse time of binary stars, or certain pulsating stars, as in our case. Deviations from periodic signals can be

<sup>2</sup> <https://archive.stsci.edu/missions/tess/doc/EXP-TESS-ARC-ICD-TM-0014.pdf>

<sup>3</sup> <https://archive.stsci.edu/missions/tess/doc/EXP-TESS-ARC-ICD-TM-0014.pdf>

used to analyze the spin-down of pulsars or to discover companions around pulsars (Wolszczan & Frail 1992; Wolszczan 1994), eclipsing binaries (Barnes & Moffett 1975), or pulsating stars (Silvotti et al. 2007, 2018; for a general review of pulsating stars in binary systems see Murphy 2018). To do so, one creates O-C (observed minus calculated) diagrams (see e.g. Sterken 2005) in order to search for deviations from the predicted ephemeris in the observations. O-C diagrams work the best if the star is pulsating in only a single mode and if the maxima are narrow and well defined, as they are easy to track in that case. However, these diagrams especially struggle with multi-mode pulsators.

#### 4.3. Frequency modulation and phase modulation: The state of the art

Building on the established methods of O-C diagrams, two new and complementary techniques have emerged for finding companions around pulsating stars. The FM method (Shibahashi & Kurtz 2012) searches and analyzes the variations in the frequency of a pulsating star induced by a companion. The periodic FM creates multiples around every pulsation peak in the frequency spectrum. Their frequencies, relative amplitudes, and phases can be used to get a full orbital solution, as described in Shibahashi et al. (2015). The effectiveness of the FM method was validated through a comparison with an eclipsing binary system (Kurtz et al. 2015), and it is best suited for data sets with a baseline that exceeds the orbital period of the companion.

The PM method is more sensitive to companions in wider orbits. It was developed by Murphy et al. (2014), Murphy & Shibahashi (2015), and Murphy et al. (2016b). Compton et al. (2016) showed that  $\delta$  Scuti stars and white dwarfs are best suited for this method. Its effectiveness was demonstrated by Schmid et al. (2015) by showing the binary nature of KIC10080943 using the PM method and attributing certain pulsations to the corresponding star in the binary due to the antiphase modulation in time delays. Such a system with observable time delays in both components is called a PB2, analogous to spectroscopic terminology, where binary star systems are called SB2s if both stars show observable RVs. Other proof of the functionality of the PM method was shown by Derekas et al. (2019) by comparing the orbital parameters derived from RV with those from PM.

An additional advantage of the PM method is its easier automation for many stars. When applying this method to 2224 main-sequence A/F stars in the 4-yr main Kepler data, Murphy et al. (2018) were able to find 317 PB1 systems, where only one component is pulsating and showing time delays, and 24 PB2 systems, where two stars are pulsating. It is worth noting here that determining orbital solutions using spectra and generating RV curves for the same number of stars would be much more time intensive.

Other methods were developed by Koen (2014) and Balona (2014) to search for binary systems by tracing the  $\delta$  Scuti pulsations of stars. In contrast to the FM and PM methods, these methods are not able to provide a full orbital solution, which is usually gained by analyzing RV curves of spectroscopic binaries.

#### 4.4. Time delays

Time delays arise when a signal (in our case always an electromagnetic wave with the propagation velocity defined by the speed of light) has to travel different distances at different epochs. Following Smart (1977) and Balona (2014), the distance

between the pulsating star and the center of gravity of its system can be described by

$$r = \frac{a_1(1 - e^2)}{1 + e \cos f}, \quad (1)$$

where  $a_1$  denotes the semi-major axis of the star,  $e$  is its eccentricity, and  $f$  is the true anomaly. The distance to the star varies relative to the Earth by

$$z = r \sin(f + \varpi) \sin i, \quad (2)$$

with  $\varpi$  being the argument of periaxis, that is, the angle between the nodal point and the periaxis<sup>4</sup>, and  $i$  as the inclination of the system.

At this point, Eq. (1) can be substituted into Eq. (2). The time delay  $\tau = -z/c$  is then completely described by the following equation:

$$\tau(t, \mathbf{x}) = -\frac{a_1 \sin i}{c} (1 - e^2) \frac{\sin f \cos \varpi + \cos f \sin \varpi}{1 + e \cos f}. \quad (3)$$

The set  $\mathbf{x} = (\Omega = 2\pi/P, a_1 \sin i/c, e, \varpi, t_p)$  in Eq. (3) includes all of the system-specific parameters needed to describe the time delay for a given time  $t$ . The term  $P$  is the orbital period of the system, or equivalently  $1/P = \nu_{\text{orb}}$  the orbital frequency, and thus  $\Omega$  is the angular orbital frequency. The projected semi-major axis of the pulsating star is described by  $a_1 \sin i$ . Dividing this quantity by the speed of light  $c$  gives us the size of the orbit for the pulsating star in light seconds. The argument of periaxis is described by  $\varpi$  and the time of periaxis passage by  $t_p$ . (For a graphical visualization of the orbital parameters, see Murphy & Shibahashi 2015.)

The two trigonometric functions of the true anomaly,  $\sin f$  and  $\cos f$ , can be expressed in terms of series expansions and Bessel functions:

$$\cos f = -e + \frac{2(1 - e^2)}{e} \sum_{n=1}^{\infty} J_n(ne) \cos n\Omega(t - t_p), \quad (4)$$

$$\sin f = 2\sqrt{1 - e^2} \sum_{n=1}^{\infty} J'_n(ne) \sin n\Omega(t - t_p), \quad (5)$$

with  $J'_n(x) = dJ_n(x)/dx$  (the derivation of Eqs. (4) and (5) can be found in Appendix A of Shibahashi et al. 2015). The changing distances between us and the clock in space are fundamentally connected with varying radial velocities,  $v_{\text{rad}}$ :

$$v_{\text{rad}} = c \frac{d\tau}{dt}. \quad (6)$$

By substituting Eq. (3) into Eq. (6), we obtain

$$v_{\text{rad}} = -\frac{\Omega a_1 \sin i}{\sqrt{1 - e^2}} [\cos(f + \varpi) + e \cos \varpi]. \quad (7)$$

<sup>4</sup> The argument of periaxis is usually denoted with  $\omega$ . This symbol, however, is used in asteroseismology to denote the angular oscillation frequency. Also, one should not confuse  $\varpi$  with the longitude of periaxis, which is the sum of the longitude of the ascending node  $\Omega$  and the argument of periaxis.

**Table 4.** Sign convention for the RV  $v_{\text{rad}}$  and the time delays  $\tau$ .

	Positive sign (+)	Negative sign (-)
$v_{\text{rad}}$	Moving away	Approaching
$\tau$	Farther away/late arrival	Closer/early arrival

Given Eq. (6) and the convention that a positive RV corresponds with a receding object and a negative RV with an approaching one, we could deduce the following: a negative time delay is due to an early arrival of the signal, that is, the star is closer to us, and vice versa<sup>5</sup> (see Table 4).

One can see in Eqs. (3) and (7) that the time delay as well as the RV of a system can be completely described by the orbital parameters. If we obtain those parameters by one method, we can predict what we should observe with the other one. Furthermore, if we generate the time delay plot from our observations, we can apply a chi-squared minimization technique in order to get the parameters in set  $\mathbf{x}$ . This concept was introduced with Murphy & Shibahashi (2015) and is a major improvement to Murphy et al. (2014), where the time delay measurements were numerically differentiated in order to derive the parameters from the obtained RV curve.

Finally, by using two of the derived orbital parameters,  $a_1 \sin i/c$  and  $P_{\text{orb}}$ , we can calculate the mass function  $f(m_1, m_2, \sin i)$  for the binary system:

$$f(m_1, m_2, \sin i) := \frac{(m_2 \sin i)^3}{(m_1 + m_2)^2} = \frac{4\pi^2 c^3}{G} v_{\text{orb}}^2 \left( \frac{a_1 \sin i}{c} \right)^3, \quad (8)$$

where  $m_2$  is the mass of the (usually non-pulsating) companion and  $G$  is the gravitational constant.

#### 4.5. Phase modulation method: Methodology

Before we could create the time delay plot, we had to analyze the change in the phase of the various pulsation modes with time. The basic equations for that can be found in Murphy et al. (2014) and are summarized in the following. We started by dividing the light curve into  $n$  equally sized segments. Then, we calculated the phase in every segment for each frequency. This left us with a series of phases  $\Phi_j$  for every segment  $(1, 2, \dots, n)$  for a fixed frequency  $\nu_j$ :

$$\Phi_j = [\phi_{1j}, \phi_{2j}, \dots, \phi_{ij}, \dots, \phi_{nj}]. \quad (9)$$

Numerically, the phase in a segment is derived by calculating the argument of the Fourier Transformation in the respective segment:

$$\Phi_j(t; \nu) = \tan^{-1} \left( \frac{\text{Im}(F(t; \nu, \delta t))}{\text{Real}(F(t; \nu, \delta t))} \right), \quad (10)$$

where  $F(t; \nu, \delta t)$  is the value of the Fourier Transformation of the time series for frequency  $\nu$  in segment  $\delta t$ .

As phases are frequency dependent, the resulting phase shifts have different amplitudes for different frequencies. To get

<sup>5</sup> This convention for the time delays was established with Murphy & Shibahashi (2015), while Murphy et al. (2014) used reversed signs; their plots are therefore mirrored around the vertical axis.

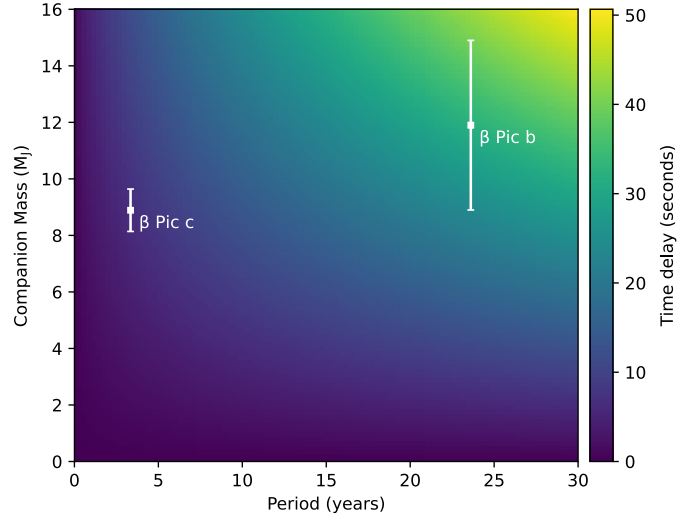


**Fig. 2.** Time delays for the  $\beta$  Pictoris system. The colors indicate the expected time delays for an edge-on planet in a circular orbit. The uncertainties in the orbital period for the planets are smaller than the marker size.

rid of this effect, we converted them into time delays by first calculating the relative phase shifts:

$$\Delta\phi_{ij} = \phi_{ij} - \bar{\phi}_j, \quad (11)$$

with  $\bar{\phi}_j$  as the mean phase of frequency  $\nu_j$ :

$$\bar{\phi}_j = \frac{1}{n} \sum_{i=1}^n \phi_{ij}. \quad (12)$$

The time delay  $\tau_{ij}$  for segment  $i$  and frequency  $\nu_j$  is thus simply the relative phase shift divided by the angular pulsation frequency:

$$\tau_{ij} = \frac{\Delta\phi_{ij}}{2\pi\nu_j}. \quad (13)$$

A planet with an orbital frequency of  $\nu_{\text{orb}}$  in a circular orbit will induce time delays that can be described by a sine function with phase  $\psi$ :

$$\tau(t) = A \sin(2\pi\nu_{\text{orb}}t + \psi). \quad (14)$$

The amplitude  $A$  can be simply derived by inserting the center of mass equation  $m_1 a_1 = m_2 a_2$  into  $\tau = a_1 \sin i/c$ :

$$\tau = \frac{a_p \sin i}{c} \frac{M_S}{M_*}, \quad (15)$$

with  $a_p$  as the semi-major axis of the companion. The terms  $M_S$  and  $M_*$  are the mass of the companion and the star, respectively. Using Eq. (15) and the mass of around  $1.8 M_\odot$  given in Table 1, we could calculate the expected time delay for a given period. This is visualized in Fig. 2. The time delay is around 24 s for  $\beta$  Pictoris b and 6 s for  $\beta$  Pictoris c. For comparison, the smallest time delay detected in the main Kepler data is 7 s (Murphy et al. 2016a).

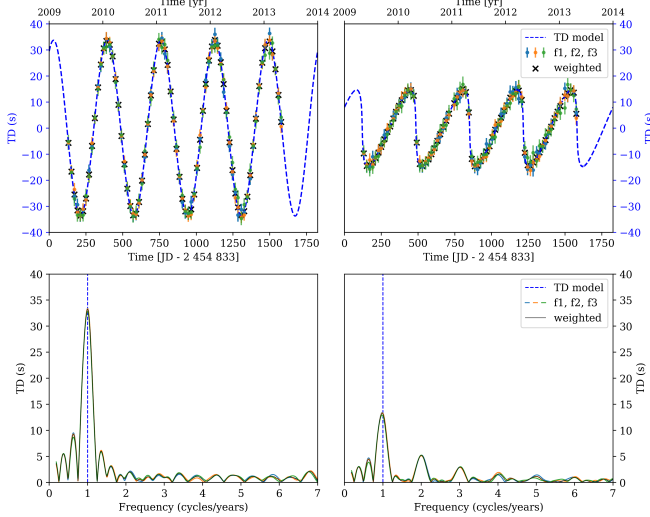


**Fig. 3.** Simulation of a companion in a circular ( $e = 0$ ; left column) and eccentric ( $e = 0.9$ ; right column) orbit as if observed by the *Kepler* Space Telescope. The following parameters were used:  $P = 1$  yr,  $\varpi = 0$ ,  $M_{\text{pulsating}} = 1.8 M_{\odot}$ , and  $M_{\text{companion}} = 0.1 M_{\odot}$ . This led to a semi-amplitude of around 34 s in the circular case (using Eq. (15)) and around 15 s in the eccentric case (using Eq. (17)). Upper panel: simulated time delay plot. Lower panel: Fourier transformation of the time delays. One can clearly see the relative increase of the first harmonic at two cycles/year for the eccentric case.

For more eccentric orbits, the pulsation time plot is described by a sum of harmonics with amplitudes  $A_k$  and phases  $\phi_k$  corresponding to order  $k$ :

$$\tau(t) = \sum_{k=1}^N A_k \sin(2\pi k v_{\text{orb}} t + \psi_k). \quad (16)$$

The height of the first harmonic relative to the one of the orbital frequency is a measure of the eccentricity. The theory behind this is described in Appendix A of Murphy et al. (2014). A visualization of that can be seen in Fig. 3. An increase in eccentricity also influences the amplitude of the time delay. This is given by the following equation:

$$\frac{a_1 \sin i}{c} = \frac{(\tau_{\max} - \tau_{\min})}{2} (1 - e^2 \cos^2 \varpi)^{-1/2}. \quad (17)$$

The maximum time delay is therefore reached in the case of  $\varpi = \pm\pi/2$  or for the simple circular orbit case.

The larger the ratio between the orbital size  $a_1 \sin i / c$  and the pulsation period  $1/\nu$ , the higher the sensitivity of the method (Murphy et al. 2016b).

Due to the size of the segments, one has to make a trade-off between time or frequency resolution. Using a shorter segment size has the advantage of a finer sensitivity at periastron; however, the uncertainties are simultaneously increased because of a poorer frequency resolution in the Fourier transform.

Under the assumption of Gaussian noise, increasing the cadence of an observation by a factor of  $N$  decreases the uncertainties in the measured phases by a factor of  $\sqrt{N}$  (Murphy 2012). The phase errors also scale inversely with amplitude, which means that the most valuable frequencies are the ones with the highest amplitudes.

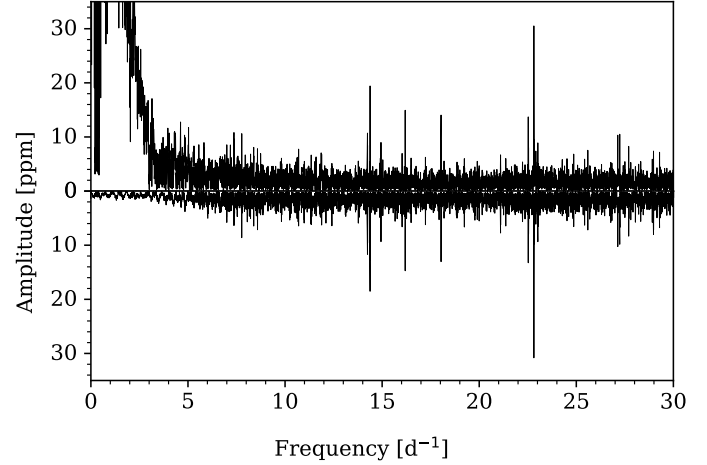


**Fig. 4.** Comparison of the amplitude spectra of the “raw” PDCSAP light curve (upper panel) and the Gaussian high-pass filtered light curve (lower panel). The power of the peaks below five  $\text{d}^{-1}$  are significantly weakened without influencing the  $\delta$  Scuti pulsations.

#### 4.6. Intrinsic amplitude and phase variations

Amplitude modulations in  $\delta$  Scuti stars have been observed in the past and thoroughly analyzed in the 4-yr main Kepler data by Bowman et al. (2016). Additionally, due to intrinsic reasons for those modulations (such as the coupling of pulsational modes or pairs of close unresolved frequencies leading to a beating effect), binarity can cause variability.

$\beta$  Pictoris is known to show amplitude variation in certain pulsational frequencies, as reported by Zwintz et al. (2019) and Mékarnia et al. (2017). However, PMs have not been observed yet (Zwintz et al. 2019).

#### 4.7. Light curve reduction

Following Murphy et al. (2016a), unused frequencies were pre-whitened from our light curves, as their presence adds unwanted variance to the data. Furthermore, a high-pass filter was applied to the light curve to remove any remaining instrumental signal and low-frequency oscillations, preserving all content at frequencies above 5  $\text{d}^{-1}$ . The effect of a high-pass filter on low frequencies can be seen in Fig. 4.

## 5. Results

To track the PM over all data sets, we started by determining which frequencies have a signal-to-noise ratio greater than four in all observations. This is the case for the four strongest frequencies in the TESS data (the first four frequencies listed in Table A.1). The stability of those frequencies over the different observations is analyzed in Sect. 5.1. We then looked at time delay curves created from simulated light curves. For this, the “best-case scenario” of a 4-yr Kepler observation of  $\beta$  Pictoris is studied in Sect. 5.2. The time delays of the real observations and a comparison to a simulated re-creation can be found in Sect. 5.3. Finally, we analyze the pulsational stability of the  $\delta$  Scuti pulsations of  $\beta$  Pictoris using TESS data in Sect. 5.5.

### 5.1. Frequency stability between the different observations

As mentioned in Sect. 4.5, the PM method derives a time delay from the observed PM at fixed frequencies. The precision with

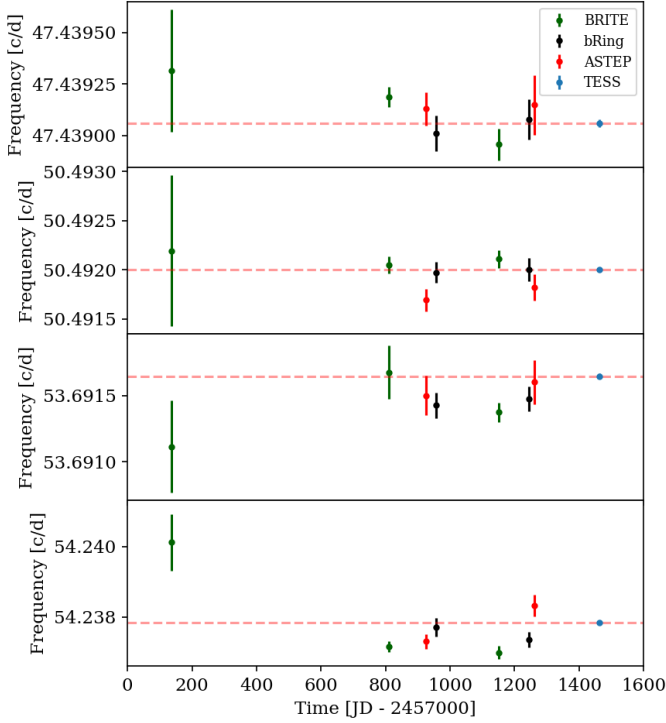


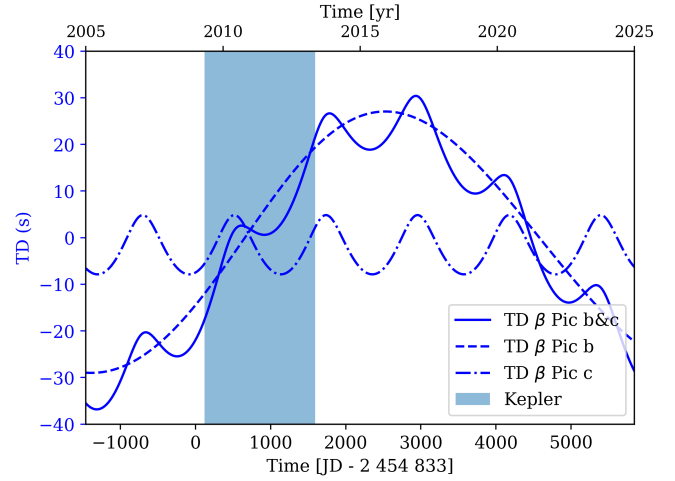
**Fig. 5.** Frequencies and their uncertainties over all data sets for the four modes that are visible in all observations from the four different observatories. The dashed red line marks the frequency determined by the TESS mission, which has the smallest uncertainties. The uncertainties were calculated following [Montgomery & Odonoghue \(1999\)](#).

which pulsational frequencies can be determined depends on the quality of the data (cadence, timebase, precision, etc.). The photometry collected by the TESS mission has the smallest uncertainties in frequency of all data sets (see Fig. 5). We therefore used TESS as a “gold standard” for the frequencies used in the PM method. The uncertainties in the frequencies were calculated following [Montgomery & Odonoghue \(1999\)](#). However, as noted in their publication, these errors are a lower limit of the true values. Keeping in mind that the actual error bars are probably bigger, one can see that the frequencies are in agreement with each other across the different data sets (Fig. 5).

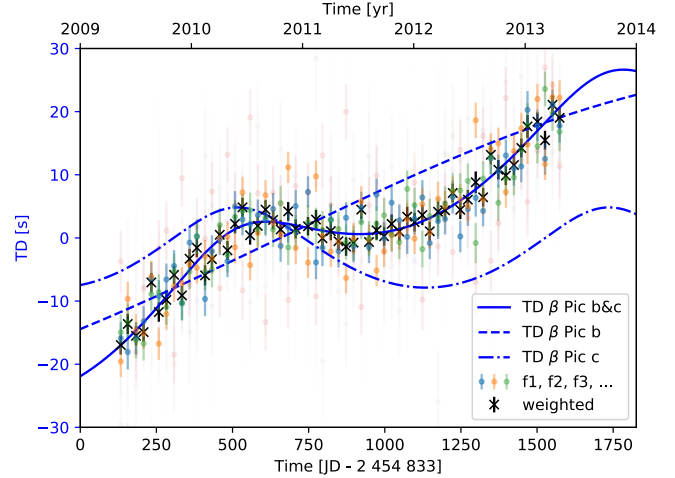
## 5.2. Simulation based on *Kepler* data

Figure 6 shows the expected time delays for  $\beta$  Pictoris caused by  $\beta$  Pictoris b and  $\beta$  Pictoris c using the full orbital solution given in Table 2. The addition of the individual contributions on the phases gives the total time delay curve as seen by the solid line in Fig. 6.

In order to see how such properties as photometric precision, cadence, and gaps in the observations influence the derived time delays, we simulated light curves of  $\beta$  Pictoris. We used the actual time stamps of the short-cadence observations of *Kepler* ([Borucki et al. 2010](#)), which have a cadence of around 1 min. The simulations consist of a multi-sine of the frequencies listed in Table A.1. Using even more frequencies increases the computational time without influencing the results of the simulations due to their low amplitudes. The time stamps were then modulated by the expected time delay at a given time using Eq. (3) and assuming a two-planet configuration in this system. Further, Gaussian noise on the order of 30 ppm was added to every data point, which is comparable to the noise floor of TESS. Following



**Fig. 6.** Expected time delays for two planets in the  $\beta$  Pictoris system. The dashed line is for  $\beta$  Pictoris b, the dash-dotted line is for  $\beta$  Pictoris c, and the solid line shows both. The blue shaded region marks the time span of *Kepler*’s 4-yr main mission; we note that *Kepler* did not observe  $\beta$  Pictoris.



**Fig. 7.** Derived time delay curve using 20-day segments by simulating *Kepler* observations of  $\beta$  Pictoris. Properties of the simulated light curve: 1-min cadence, continuous observations, 20 ppm noise in flux. The strongest frequencies ( $f_1, f_2, f_3, \dots$ ) are shown here with their uncertainties. The weighted average of the measurements is shown in black.

the procedure explained in Sect. 4.5, the light curve was separated into 20-day segments, and the time delays were calculated from the phases in every segment with a fixed frequency. Finally, we calculated weighted time delay values and their corresponding uncertainties using the first three frequencies with the highest amplitudes.

The first simulation (Fig. 7) used the *Kepler* short-cadence 1-min time stamps. The measured time delays follow the prediction for a two-planet case. Removing every second data point, which effectively reduces the number of measurements by 50%, does not change the result (Fig. 8). One can, however, observe a small increase in the uncertainties for the time delays. This is expected, as a decrease of data points by a factor of two increases the uncertainty by a factor of  $\sqrt{2}$ , assuming Gaussian noise ([Murphy 2012](#)). Finally, we induced gaps into the light curve, effectively simulating ground-based observations by having data only for

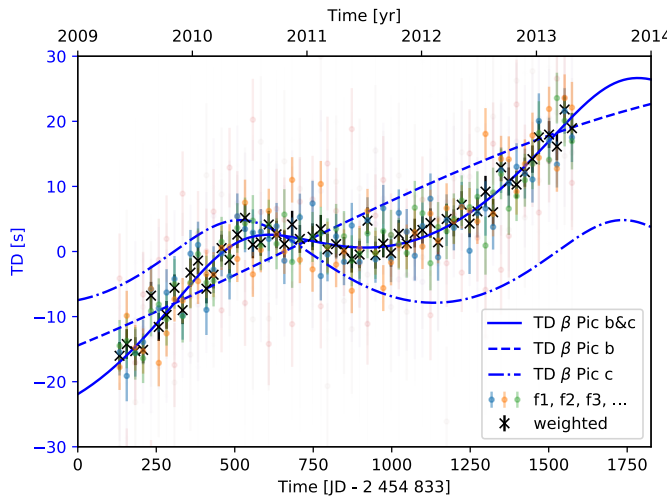


**Fig. 8.** Derived time delay curve using 20-day segments by simulating *Kepler* observations of  $\beta$  Pictoris. Properties of the simulated light curve: 2-min cadence, continuous observations, 20 ppm noise in flux.

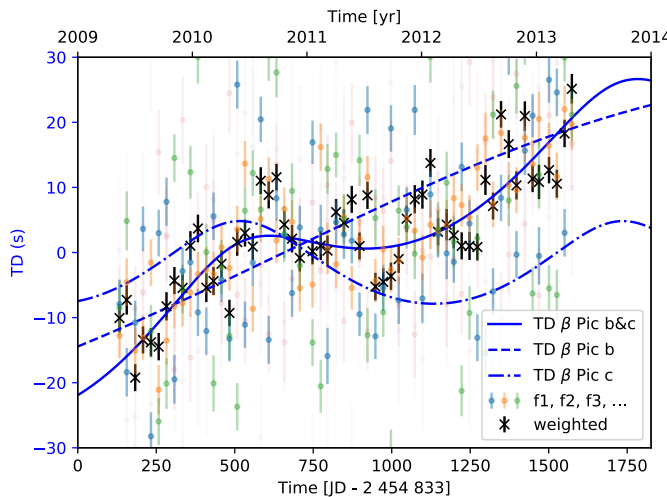


**Fig. 9.** Derived time delay curve using 20-day segments by simulating *Kepler* observations of  $\beta$  Pictoris. Properties of the simulated light curve: 1-min cadence, 0.5-day gaps every day, 20 ppm noise in flux.

half of the day. Due to a worse spectral window, there are many more peaks present in the amplitude spectrum. These new peaks influence the phases for the observed frequencies, as they cannot be resolved anymore. The scatter in the time delays increases significantly (Fig. 9), and one cannot conclusively distinguish between a one-planet solution (only  $\beta$  Pictoris b) or a two-planet solution. A bigger segment size mitigates this effect, as expected by the Rayleigh criterion.

This clearly illustrates that gaps influence the time delays the strongest, as the uncertainties in phase only scale with the square root of the cadence factor. One should also remove identified frequencies that are not used in the time delay analysis to get rid of their aliases.

### 5.3. Time delay analysis of the photometry

Figure 10 shows the predicted time delays caused by the planets in the  $\beta$  Pictoris system during the times when the observatories

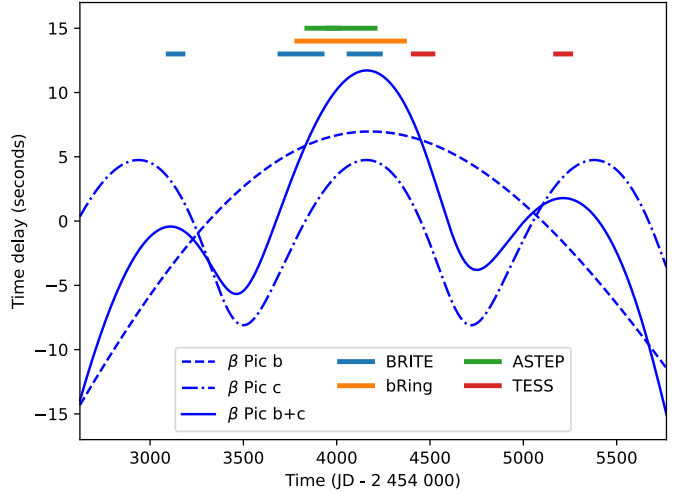


**Fig. 10.** Time delay predictions for  $\beta$  Pictoris b (dashed line), c (dashed-dotted line), and both planets (solid line). Times when the star was observed are marked with lines.

BRITE, ASTEP, bRing, and TESS collected photometry for the star. The available observations have been introduced in Sect. 3. The semi-amplitude of the predicted time delays for  $\beta$  Pictoris b and c is around 24 and 6 s, respectively.

As seen in Sect. 5.1, the TESS observations show the smallest uncertainties in frequency and were therefore used as a “gold standard” in this analysis. The frequency was thus fixed to the TESS values, as the PM method observes the phase shifts at a constant frequency (see Sect. 4.5). The time delay predictions (blue lines in Figs. 10–12) were also normalized to the midpoint time of TESS. As a time delay is a relative measure and not an absolute one, we set the time delay for TESS to zero. The evaluated time delays shown in Figs. 11 and 12 are therefore relative to the TESS values.

The code used to calculate the time delays was written for this analysis and is heavily based on existing ones, namely `timedelay`<sup>6</sup> and `maelstrom`<sup>7</sup> (Hey et al. 2020a). The equations that were needed in order to evaluate the time delays are given in Sects. 4.4 and 4.5.

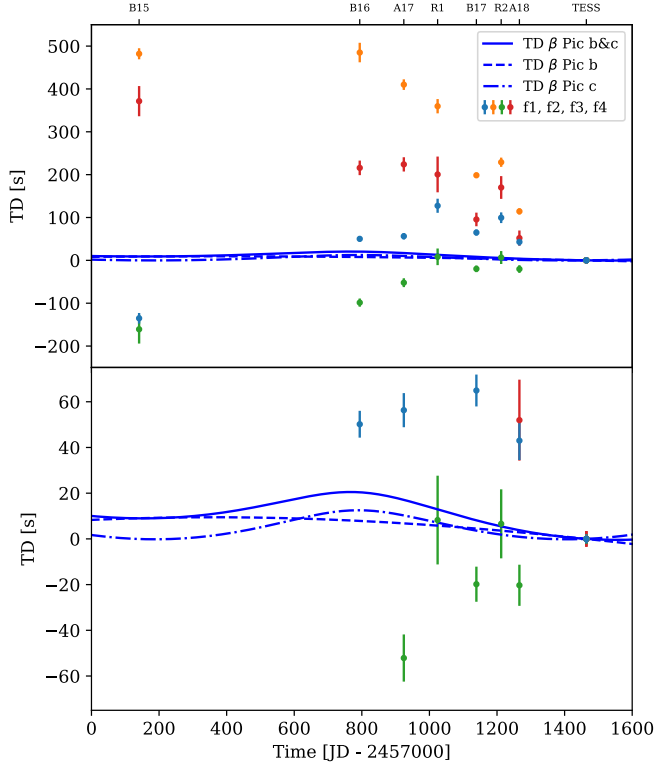
The phases were calculated by subtracting the midpoint time of the full data set. As discussed in Sect. 5.1, there are only four frequencies that are significant in all observations. The phases for each data set were then calculated based on a least-squares routine and their uncertainties from the respective covariance matrices. Equation (13) gives the conversion between the phase of a frequency and the respective time delays.

Figure 11 shows the derived time delays for the four different frequencies. They are clearly not consistent with each other. As discussed in Sect. 4.6, this rules out an extrinsic cause for the modulations (e.g., a companion), as all frequencies would show a similar behavior (examples of this are shown in Figs. 3, 7, 8 and 9). A change in frequency was ruled out in Sect. 5.1. Furthermore, Zwintz et al. (2019) showed no significant phase change for our four frequencies in the BHr 2018 data set (therein, these four frequencies have the designations F8, F11, F13, and F15).

Next, we attempted to reproduce the different data sets as faithfully as possible and compare them with the time delay values shown in Fig. 11. For that, we first determined the frequency, amplitude, and phase of the four pulsation modes visible

<sup>6</sup> <https://github.com/danhey/timedelay>

<sup>7</sup> <https://github.com/danhey/maelstrom>



**Fig. 11.** Time delay plot calculated from the phases of four different frequencies for all available observations by BRITE, bRing, ASTEP and TESS. Each color represents a frequency ( $f_1, f_2, f_3$ , and  $f_4$ ) listed in Table A.1. The blue lines indicate time delay predictions for  $\beta$  Pictoris b (dashed line), c (dashed, dotted line), and both planets (solid line). The lower panel is a zoom-in of the upper panel. The uncertainties in the time delays were derived from the covariance matrices given by the least-squares procedure, which was used in order to calculate the phases of the respective frequencies. The ticks at the top of the plot denote the various observatories: B15, B16, and B17 for the BRITE observations in the years 2015, 2016, and 2017, respectively; A17 and A18 for the ASTEP observations in 2017 and 2018; and R1 and R2 for the first and second part of the bRing data.

in all observations. We calculated the residual noise for the pre-whitened data sets, which was then used to estimate the uncertainties following Montgomery & Odonoghue (1999). As before, we fixed the frequency to the TESS value. As we do not know the exact “true” frequency of the pulsations with infinite precision, we introduced an offset between the true pulsational frequencies and the TESS data set in the simulations. The uncertainty in frequency for these four strongest frequencies is on the order of  $10^{-5}$  day $^{-1}$  (see Table A.1). This offset explains the linear trend for every frequency that is visible in Fig. 11. The time delays of the simulated data set are shown in Fig. 12.

This linear trend was discussed on simulated data in Sect. 3.2 of Murphy et al. (2016b) and “almost certainly” explains the observed trend in the WASP data of Murphy et al. (2013). A way to correct for it is to evaluate the slope between two maxima or minima of the sinusoidal variations. This is not a possibility in our case, as we would have had to further segment the data sets to identify the position of the maxima or minima, leading to even higher scatter in the phase. The lower panel of Fig. 11 also shows that the uncertainties in the derived time delays for the data sets other than TESS are too big to differentiate between a one-planet or two-planet scenario, even without this linear

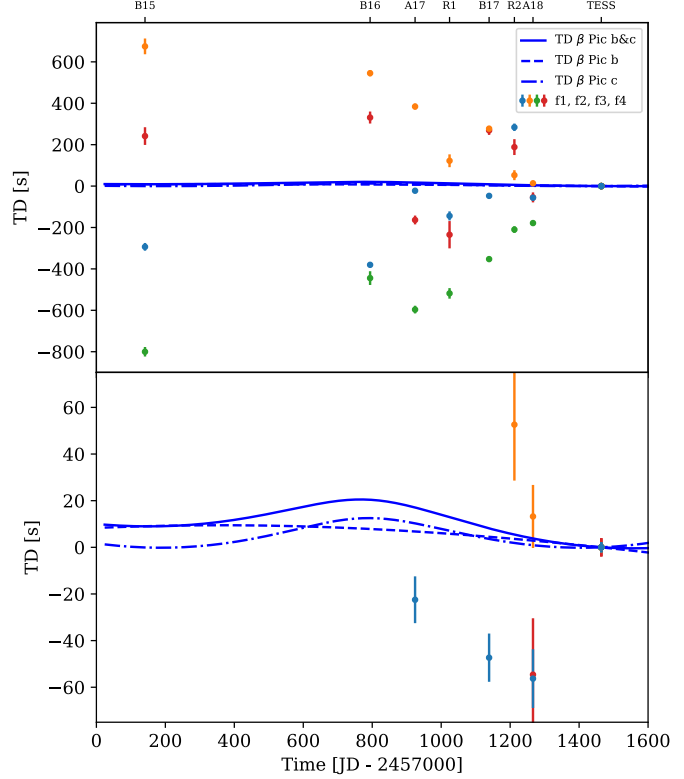


**Fig. 12.** Time delay plot for the simulated data set showing a high similarity to the time delays of the real data set presented in Fig. 12. The colored points represent the simulated time delays for the four strongest pulsational frequencies. The blue lines indicate time delay predictions for  $\beta$  Pictoris b (dashed line), c (dashed-dotted line), and both planets (solid line). The lower panel is a zoom-in of the upper panel. A description of the ticks at the top of the plot can be found in the caption of Fig. 11.

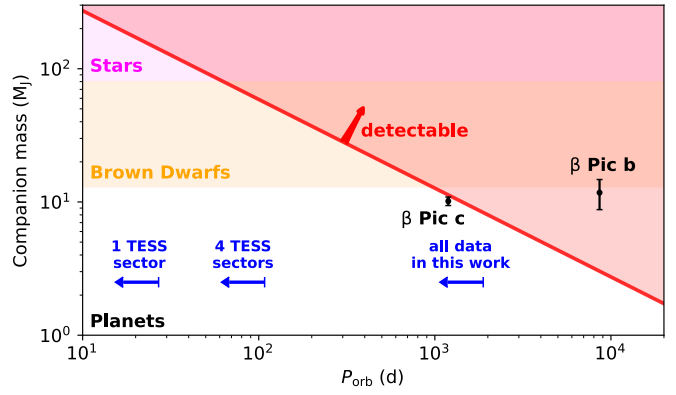


**Fig. 13.** Detection limits for the  $\beta$  Pictoris system based on the calculations presented in Hey et al. (2020b) assuming  $1.8 M_{\odot}$  for the star and an inclination of  $90^{\circ}$  for both planets. The detectable parameter space for companions depending on their orbital period  $P_{\text{orb}}$  and mass is shaded red, assuming  $\beta$  Pictoris is a non-ideal  $\delta$  Scuti pulsator (see Sect. 5.5 for a discussion on the pulsational modes of  $\beta$  Pictoris as seen by TESS).  $\beta$  Pictoris c is generally not detectable due to the intrinsic noise of the pulsations, and the time delay caused by  $\beta$  Pictoris b has a period that is too long in comparison to the baseline of our observations. The masses corresponding to brown dwarfs ( $13 M_{\text{J}} \lesssim M \lesssim 80 M_{\text{J}}$ ) are shaded in yellow, and the stellar regime ( $M > 80 M_{\text{J}}$ ) is in magenta, with  $M_{\text{J}}$  being a Jupiter mass. The figure is adapted from Hey et al. (2020b).

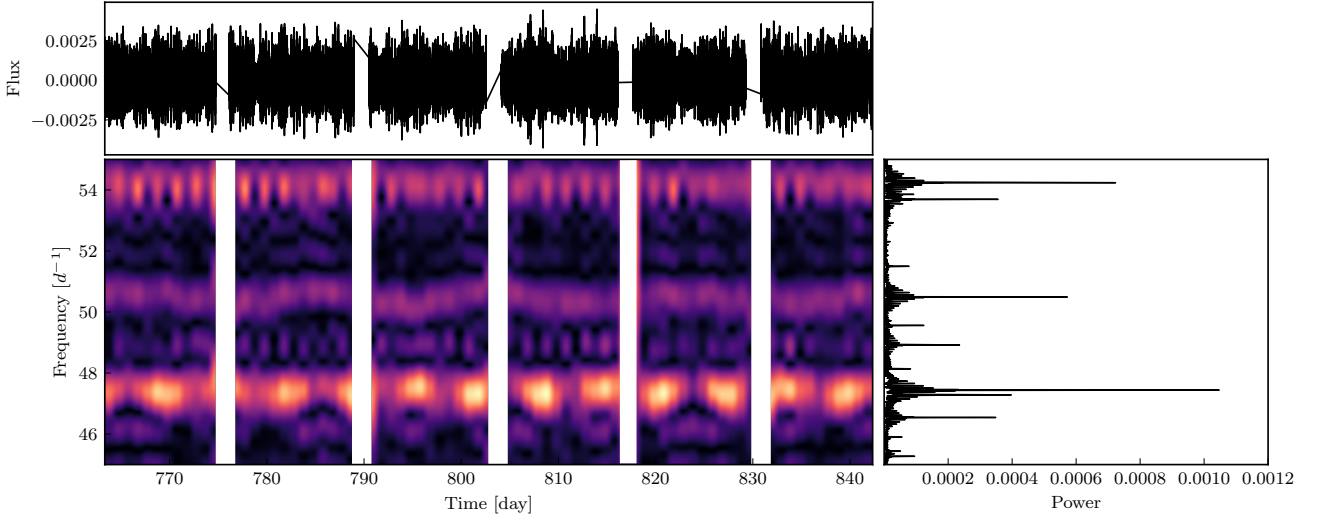


**Fig. 14.** Two-dimensional periodogram showing the frequency region between  $45$  and  $55$   $\text{day}^{-1}$ . One can see that most of the modes are significantly amplitude modulated by the rotational signal. The mode at  $54$   $\text{day}^{-1}$  goes much faster, which is probably due to beating with nearby modes. The mode at  $50.5$   $\text{day}^{-1}$  itself undergoes incoherent FM.

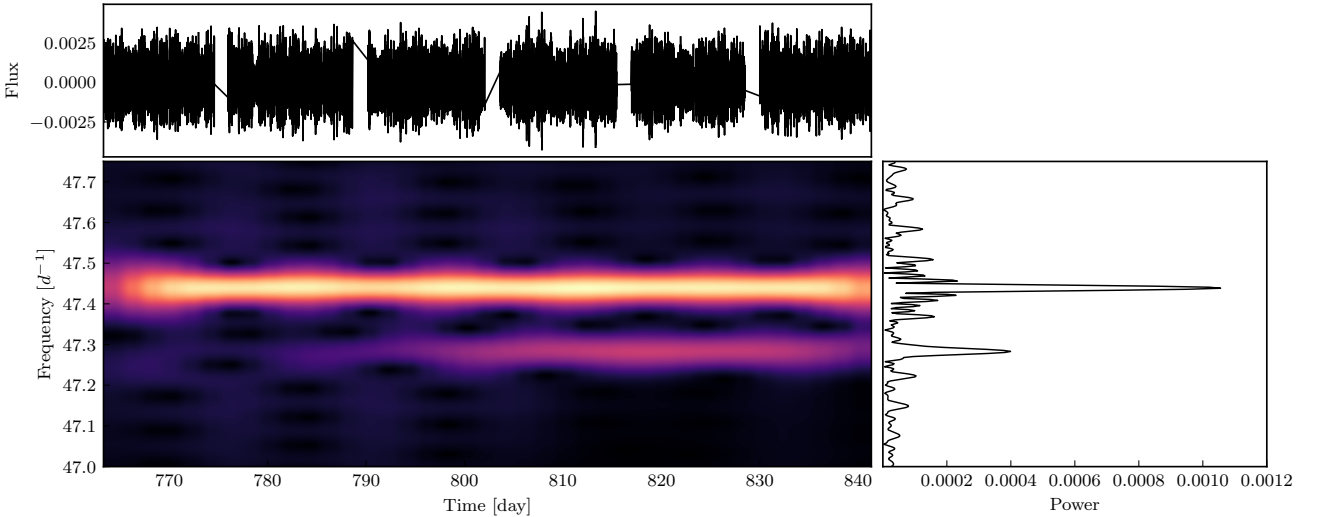


**Fig. 15.** Periodogram showing a pulsational mode around  $47.3$   $\text{day}^{-1}$  that is just appearing at the end of the observations.

trend. We therefore discuss the possibility of a second  $\beta$  Pictoris observation by TESS in the extended mission in the next section.

#### 5.4. Detection limits for $\beta$ Pictoris

Here, we determine the detection limits for companions in the  $\beta$  Pictoris system using the PM method. In a prior study by Hey et al. (2020b), the authors tried to estimate the detection limits of companions around  $\delta$  Scuti stars. Their approach involved simulating time-series observations of these pulsating stars and adding white noise to the data. This allowed them to find a relationship between the S/N of the stellar pulsations and the observed scatter in the resulting time delay ( $a \sin i/c$ ). The established relationship could be directly converted into a parameter space defining detectable companion masses and their orbital periods. The authors found that the detectability of companions strongly depends on the S/N of the stellar pulsations. Given the comparably low observed S/N of the  $\delta$  Scuti pulsations observed in  $\beta$  Pictoris and the instability of the pulsational modes, we

opted for a more conservative detection limit than what (84th percentile in Hey et al. 2020b) presented in their prior work.

Our findings are presented in Fig. 13. We determined that the intrinsic variability of  $\beta$  Pictoris is too high to detect planet c. The other companion,  $\beta$  Pictoris b, is primarily not detectable at the moment due to the short baseline of observations compared to its long orbital period of approximately 24 yr. It is worth noting that these calculations assume that the pulsational modes stay stable during the time of observations. However, we show in Sect. 5.5 by using the TESS data that this assumption is generally not met, with some modes appearing and disappearing during the observations. This further complicates any efforts to detect companions around the star.

#### 5.5. Analysis of pulsational stability using TESS data

$\beta$  Pictoris was observed in seven individual sectors between October 2018 and February 2021 (see Table 3). We performed a frequency analysis of these TESS sectors using `maelstrom`. We find that  $\beta$  Pictoris is seemingly undergoing significant

frequency and amplitude modulation, which buries any signal induced by planetary companions. The periodograms of the stellar pulsations clearly show significant amplitude modulation by the rotational signal (see Fig. 14). We also find that the star is showing modes that are appearing and disappearing on short timescales. Figure 15 shows a mode that seems to be just appearing during the second half of the TESS observations. In summary, we find that  $\beta$  Pictoris' modes are not stable enough to probe to the necessary phase precision for the planetary companions.

### 5.6. Comparison to KIC 7917485

Here, we compare the  $\beta$  Pictoris system to another A star with a planet detected through pulsation timing, KIC 7917485 (Murphy et al. 2016a), and evaluate the differences between the host stars that have affected the detectability of their corresponding planets. Compared to other *Kepler*  $\delta$  Scuti stars, including those with binary star companions, (e.g., Murphy et al. 2018, 2020a), and Murphy et al. (2016a) found that KIC 7917485 had an exceptionally low time delay noise (sixth lowest of the 2040  $\delta$  Scuti stars in the *Kepler* primary mission sample). Similar planetary-mass companions might exist around the second and ninth lowest noise stars in the *Kepler* sample (KIC 9700322 and KIC 8453431). Unlike KIC 7917485, however, the observations of these systems and their potential companions do not cover a full orbital period, thus precluding determination of their orbital parameters.

The additional time-delay jitter seen in  $\beta$  Pictoris might arise from mode interaction or from other effects causing the observed changes in mode amplitude. It is this jitter that hinders the ability to detect planetary-mass objects around pulsating stars. This is comparable to the intrinsic RV jitter of a star, which impacts the ability to detect planets using RV measurements. The intrinsic variability is evident in the  $\delta$  Scuti pulsations of  $\beta$  Pictoris and generally renders white dwarfs and subdwarfs as less ideal targets for the analysis of their time delays using the PM method (Murphy 2018). This limitation persists despite the high oscillation frequencies exhibited by these pulsating stars that would otherwise make them promising targets for detecting time delays caused by a companion (Compton et al. 2016).

## 6. Conclusions

In this work, we have analyzed the time delays derived from the phases of the  $\delta$  Scuti pulsations of  $\beta$  Pictoris. The photometric data of the star were collected over a time period of approximately 4 yr by four different observatories: the BRITE-Constellation, bRing, ASTEP, and TESS. In contrast to previous studies, we did not segment the observations into smaller sets (e.g. ten-day bins). This would have caused high uncertainties in the phases and therefore also in the time delays. Nevertheless, we could not see the influence of  $\beta$  Pictoris b or c in the data due to this time delay scatter. The uncertainty in the pulsational frequencies leads to a linear trend in the time delays and has also been seen in a previous study by Murphy et al. (2013) and in simulations by Murphy et al. (2016b). We performed a frequency analysis using the open-source tool `maelstrom`. We find that  $\beta$  Pictoris does not have the needed stability to detect planetary companions using the time delay method. The stellar pulsations clearly show strong amplitude modulation caused by the rotational signal and identify modes that seemingly appeared during our observations.

Previous studies have used the PM method on *Kepler* data, finding many binary star systems (Murphy et al. 2016b, and references therein) and a planet (Murphy et al. 2016a). This work is the first to use the PM method with so many different data sets that have a precision significantly lower than the *Kepler* mission. However, the PM method remains valuable technique, as it is able to find planets and stars in a parameter space that is poorly covered by other methods, such as the RV method (see e.g. Murphy 2018).

*Acknowledgements.* This work includes data collected by the TESS mission, which are publicly available from the Mikulski Archive for Space Telescopes (MAST). Funding for the TESS mission is provided by the NASA Explorer Program. This work has made use of data from the European Space Agency (ESA) mission *Gaia* (<https://www.cosmos.esa.int/gaia>), processed by the *Gaia* Data Processing and Analysis Consortium (DPAC, <https://www.cosmos.esa.int/web/gaia/dpac/consortium>). Funding for the DPAC has been provided by national institutions, in particular the institutions participating in the *Gaia* Multilateral Agreement. We made use of the software package `Period04` (Lenz & Breger 2005), the Python programming language (Rossum 1995), and the open-source Python packages `numpy` (van der Walt et al. 2011), `matplotlib` (Hunter 2007), `astropy` (Astropy Collaboration 2013), `lightkurve` (Lightkurve Collaboration 2018), `timedelay`<sup>8</sup>, `maelstrom`<sup>9</sup> and `SMURFS` (Müller 2020). This research has made use of the SIMBAD database, operated at CDS, Strasbourg, France. This research has made use of the NASA Exoplanet Archive, which is operated by the California Institute of Technology, under contract with the National Aeronautics and Space Administration under the Exoplanet Exploration Program. Part of this research was carried out at the Jet Propulsion Laboratory, California Institute of Technology, under a contract with the National Aeronautics and Space Administration (80NM0018D0004). This research has made use of data collected by the BRITE-Constellation satellite mission, designed, built, launched, operated and supported by the Austrian Research Promotion Agency (FFG), the University of Vienna, the Technical University of Graz, the University of Innsbruck, the Canadian Space Agency (CSA), the University of Toronto Institute for Aerospace Studies (UTIAS), the Foundation for Polish Science & Technology (FNITP MNiSW), and National Science Centre (NCN). The bRing observatory at Siding Springs, Australia was supported by a University of Rochester University Research Award. The field activities at Dome C for ASTEP benefit from the support of the French and Italian polar agencies IPEV and PNRA in the framework of the Concordia station programme. The PicSat team thanks funding from the European Research Council (ERC) under the Horizon 2020 research and innovation programme (Grant agreement No. 639248, LITHIUM). SJM was supported by the Australian Research Council (ARC) through Future Fellowship FT210100485.

## References

Abe, L., Gonçalves, I., Agabi, A., et al. 2013, *A&A*, **553**, A49  
 Aerts, C., Christensen-Dalsgaard, J., & Kurtz, D. W. 2010, *Asteroseismology* (Dordrecht: Springer)  
 Antoci, V., Cunha, M., Houdek, G., et al. 2014, *ApJ*, **796**, 118  
 Astropy Collaboration (Robitaille, T. P., et al.) 2013, *A&A*, **558**, A33  
 Augereau, J. C., Nelson, R. P., Lagrange, A. M., Papaloizou, J. C. B., & Mouillet, D. 2001, *A&A*, **370**, 447  
 Aumann, H. H., Gillett, F. C., Beichman, C. A., et al. 1984, *ApJ*, **278**, L23  
 Balona, L. A. 2014, *MNRAS*, **443**, 1946  
 Barnes, T. G., I., & Moffett, T. J. 1975, *AJ*, **80**, 48  
 Bedding, T. R., Murphy, S. J., Hey, D. R., et al. 2020, *Nature*, **581**, 147  
 Beust, H., & Morbidelli, A. 2000, *Icarus*, **143**, 170  
 Blunt, S., Wang, J. J., Angelo, I., et al. 2020, *AJ*, **159**, 89  
 Borucki, W. J., Koch, D., Basri, G., et al. 2010, *Science*, **327**, 977  
 Bowman, D. M., Kurtz, D. W., Breger, M., Murphy, S. J., & Holdsworth, D. L. 2016, *MNRAS*, **460**, 1970  
 Breger, M., & Montgomery, M. H. 2014, *ApJ*, **783**, 89  
 Breger, M., Stich, J., Garrido, R., et al. 1993, *A&A*, **271**, 482  
 Burrows, C. J., Krist, J. E., Stapelfeldt, K. R., & WFPC2 Investigation Definition Team. 1995, in *American Astronomical Society Meeting Abstracts*, 187, 32.05  
 Compton, D. L., Bedding, T. R., Murphy, S. J., & Stello, D. 2016, *MNRAS*, **461**, 1943  
 Cousins, A. W. J. 1971, *Roy. Observ. Ann.*, **7**

<sup>8</sup> <https://github.com/danhey/timedelay>

<sup>9</sup> <https://github.com/danhey/maelstrom>

Derekas, A., Murphy, S. J., Dálya, G., et al. 2019, *MNRAS*, **486**, 2129

Perlet, R., Hobbs, L. M., & Madjar, A. V. 1987, *A&A*, **185**, 267

Gaia Collaboration (Prusti, T., et al.) 2016, *A&A*, **595**, A1

Gaia Collaboration (Vallenari, A., et al.) 2023, *A&A*, **674**, A1

Galland, F., Lagrange, A. M., Udry, S., et al. 2006, *A&A*, **447**, 355

Golimowski, D. A., Ardila, D. R., Krist, J. E., et al. 2006, *AJ*, **131**, 3109

Gray, R. O., Corbally, C. J., Garrison, R. F., et al. 2006, *AJ*, **132**, 161

Guillot, T., Abe, L., Agabi, A., et al. 2015, *Astron. Nachr.*, **336**, 638

Heap, S. R., Lindler, D. J., Lanz, T. M., et al. 2000, *ApJ*, **539**, 435

Hermes, J. J. 2018, *Timing by Stellar Pulsations as an Exoplanet Discovery Method* (Cham: Springer), 6

Hey, D., Murphy, S., Foreman-Mackey, D., et al. 2020a, *J. Open Source Softw.*, **5**, 2125

Hey, D. R., Murphy, S. J., Foreman-Mackey, D., et al. 2020b, *AJ*, **159**, 202

Hogg, D. W., Bovy, J., & Lang, D. 2010, arXiv e-prints [arXiv:1008.4686]

Houdek, G. 2000, in *Delta Scuti and Related Stars*, eds. M. Breger, & M. Montgomery, *Astronomical Society of the Pacific Conference Series*, **210**, 454

Hunter, J. D. 2007, *Comput. Sci. Eng.*, **9**, 90

Jenkins, J. M. 2017, *Kepler Data Processing Handbook: Overview of the Science Operations Center*, Tech. rep., NASA Ames Research Center

Jenkins, J. M., Caldwell, D. A., Chandrasekaran, H., et al. 2010, *ApJ*, **713**, L87

Jenkins, J. M., Twicken, J. D., McCauliff, S., et al. 2016, *SPIE Conf. Ser.*, **9913**, 99133E

Kalas, P., Zwintz, K., Kenworthy, M., et al. 2019, in *American Astronomical Society Meeting Abstracts*, **233**, 218.03

Kanodia, S., & Wright, J. T. 2018, *Barycorpy: Barycentric velocity calculation and leap second management* Astrophysics Source Code Library, [record ascl:1808.001]

Kenworthy, M. 2017, *Nat. Astron.*, **1**, 0099

Kenworthy, M. A., Mellon, S. N., Bailey, J. I., et al. 2021, *A&A*, **648**, A15

Koen, C. 2003, *MNRAS*, **341**, 1385

Koen, C. 2014, *MNRAS*, **444**, 1486

Kurtz, D. W., Hambleton, K. M., Shibahashi, H., Murphy, S. J., & Prša, A. 2015, *MNRAS*, **446**, 1223

Lacour, S., Wang, J. J., Rodet, L., et al. 2021, *A&A*, **654**, A2

Lagrange, A. M., Desort, M., Galland, F., Udry, S., & Mayor, M. 2009a, *A&A*, **495**, 335

Lagrange, A. M., Gratadour, D., Chauvin, G., et al. 2009b, *A&A*, **493**, L21

Lagrange, A. M., Bonnefoy, M., Chauvin, G., et al. 2010, *Science*, **329**, 57

Lagrange, A. M., De Bondt, K., Meunier, N., et al. 2012, *A&A*, **542**, A18

Lagrange, A. M., Boccaletti, A., Langlois, M., et al. 2019a, *A&A*, **621**, L8

Lagrange, A. M., Meunier, N., Rubini, P., et al. 2019b, *Nat. Astron.*, **421**

Lagrange, A. M., Rubini, P., Nowak, M., et al. 2020, *A&A*, **642**, A18

Lecavelier des Etangs, A., & Vidal-Madjar, A. 2016, *A&A*, **588**, A60

Lecavelier Des Etangs, A., Deleuil, M., Vidal-Madjar, A., et al. 1995, *A&A*, **299**, 557

Lecavelier des Etangs, A., Cros, L., Hébrard, G., et al. 2022, *Sci. Rep.*, **12**, 5855

Lenz, P., & Breger, M. 2005, *Commun. Asteroseismol.*, **146**, 53

Lightkurve Collaboration (Cardoso, J. V. d. M., et al.) 2018, *Lightkurve: Kepler and TESS time series analysis in Python* Astrophysics Source Code Library, [record ascl:1812.013]

Lindgren, L., Klioner, S. A., Hernández, J., et al. 2021, *A&A*, **649**, A2

Lomb, N. R. 1976, *Astrophys. Space Sci.*, **39**, 447

Mamajek, E. E., & Bell, C. P. M. 2014, *MNRAS*, **445**, 2169

Mékarnia, D., Chapellier, E., Guillot, T., et al. 2017, *A&A*, **608**, A6

Mellon, S. N., Mamajek, E. E., Stuik, R., et al. 2019, *ApJS*, **244**, 15

Menegaldo, C. G., de O. Fialho, F., Janot-Pacheco, E., Pait, F. M., & Lapeyrère, V. 2022, *PASP*, **134**, 034501

Montgomery, M. H., & Odonoghue, D. 1999, *Delta Scuti Star Newsletter*, **13**, 28

Mouillet, D., Larwood, J. D., Papaloizou, J. C. B., & Lagrange, A. M. 1997, *MNRAS*, **292**, 896

Müllner, M. 2020, , <https://doi.org/10.5281/zenodo.3635801>

Murphy, S. J. 2012, *MNRAS*, **422**, 665

Murphy, S. J. 2018, arXiv e-prints [arXiv:1811.12659]

Murphy, S. J., & Shibahashi, H. 2015, *MNRAS*, **450**, 4475

Murphy, S. J., Pigulski, A., Kurtz, D. W., et al. 2013, *MNRAS*, **432**, 2284

Murphy, S. J., Bedding, T. R., Shibahashi, H., Kurtz, D. W., & Kjeldsen, H. 2014, *MNRAS*, **441**, 2515

Murphy, S. J., Bedding, T. R., & Shibahashi, H. 2016a, *ApJ*, **827**, L17

Murphy, S. J., Shibahashi, H., & Bedding, T. R. 2016b, *MNRAS*, **461**, 4215

Murphy, S. J., Moe, M., Kurtz, D. W., et al. 2018, *MNRAS*, **474**, 4322

Murphy, S. J., Barbara, N. H., Hey, D., Bedding, T. R., & Fulcher, B. D. 2020a, *MNRAS*, **493**, 5382

Murphy, S. J., Saio, H., Takada-Hidai, M., et al. 2020b, *MNRAS*, **498**, 4272

Murphy, S. J., Joyce, M., Bedding, T. R., White, T. R., & Kama, M. 2021, *MNRAS*, **502**, 1633

Nesvold, E. R., & Kuchner, M. J. 2015, *ApJ*, **798**, 83

Nowak, M., Lacour, S., Crouzier, A., et al. 2018, *SPIE Conf. Ser.*, **10698**, 1069821

Nowak, M., Lacour, S., Lagrange, A. M., et al. 2020, *A&A*, **642**, L2

Pavlenko, Y., Kulyk, I., Shubina, O., et al. 2022, *A&A*, **660**, A49

Popowicz, A., Pigulski, A., Bernacki, K., et al. 2017, *A&A*, **605**, A26

Ricker, G. R., Winn, J. N., Vanderspek, R., et al. 2015, *J. Astron. Telescopes Instrum. Syst.*, **1**, 014003

Rossum, G. 1995, *Python Reference Manual*, Tech. rep., Centrum voor Wiskunde en Informatica (CWI), Amsterdam, The Netherlands

Scargle, J. D. 1982, *ApJ*, **263**, 835

Schmid, V. S., Tkachenko, A., Aerts, C., et al. 2015, *A&A*, **584**, A35

Shibahashi, H., & Kurtz, D. W. 2012, *MNRAS*, **422**, 738

Shibahashi, H., Kurtz, D. W., & Murphy, S. J. 2015, *MNRAS*, **450**, 3999

Silvotti, R., Schuh, S., Janulis, R., et al. 2007, *Nature*, **449**, 189

Silvotti, R., Schuh, S., Kim, S. L., et al. 2018, *A&A*, **611**, A85

Smart, W. M. 1977, *Textbook on Spherical Astronomy*, 6th edn. (Cambridge University Press)

Smith, B. A., & Terrile, R. J. 1984, *Science*, **226**, 1421

Smith, J. C., Stumpe, M. C., Van Cleve, J. E., et al. 2012, *PASP*, **124**, 1000

Snellen, I. A. G., Stuik, R., Navarro, R., et al. 2012, *SPIE Conf. Ser.*, **8444**, 844401

Stassun, K. G., Oelkers, R. J., Paegert, M., et al. 2019, *AJ*, **158**, 138

Steindl, T., Zwintz, K., & Müllner, M. 2022, *A&A*, **664**, A32

Sterken, C. 2005, in *The Light-Time Effect in Astrophysics: Causes and Cures of the O-C Diagram*, ed. C. Sterken, *Astronomical Society of the Pacific Conference Series*, **335**, 3

Strøm, P. A., Bodewits, D., Knight, M. M., et al. 2020, *PASP*, **132**, 101001

Stuik, R., Bailey, J. I., Dorval, P., et al. 2017, *A&A*, **607**, A45

Stumpe, M. C., Smith, J. C., Van Cleve, J. E., et al. 2012, *PASP*, **124**, 985

Talens, G. J. J., Albrecht, S., Spronck, J. F. P., et al. 2017, *A&A*, **606**, A73

Talens, G. J. J., Deul, E. R., Stuik, R., et al. 2018, *A&A*, **619**, A154

van der Walt, S., Colbert, S. C., & Varoquaux, G. 2011, *Comput. Sci. Eng.*, **13**, 22

Wang, J. J., Graham, J. R., Pueyo, L., et al. 2016, *AJ*, **152**, 97

Weiss, W. W., Rucinski, S. M., Moffat, A. F. J., et al. 2014, *PASP*, **126**, 573

Wolszczan, A. 1994, *Science*, **264**, 538

Wolszczan, A., & Frail, D. A. 1992, *Nature*, **355**, 145

Wright, J. T., & Eastman, J. D. 2014, *PASP*, **126**, 838

Zieba, S., Zwintz, K., Kenworthy, M. A., & Kennedy, G. M. 2019, *A&A*, **625**, A13

Zwintz, K., Fossati, L., Ryabchikova, T., et al. 2014, *Science*, **345**, 550

Zwintz, K., Reese, D. R., Neiner, C., et al. 2019, *A&A*, **627**, A28

<sup>1</sup> Max-Planck-Institut für Astronomie, Königstuhl 17, 69117 Heidelberg, Germany  
e-mail: zieba@mpia.de

<sup>2</sup> Leiden Observatory, Leiden University, Postbus 9513, 2300 RA Leiden, The Netherlands

<sup>3</sup> Institut für Astro- und Teilchenphysik, Universität Innsbruck, Technikerstraße 25, 6020 Innsbruck, Austria

<sup>4</sup> Institute for Astronomy, University of Hawai‘i, Honolulu, HI 96822, USA

<sup>5</sup> Centre for Astrophysics, University of Southern Queensland, Toowoomba, QLD 4350, Australia

<sup>6</sup> Institut für Physik, Karl-Franzens Universität Graz, Universitätsplatz 5/II, NAWI Graz, 8010 Graz, Austria

<sup>7</sup> Université Côte d’Azur, Observatoire de la Côte d’Azur, CNRS, Laboratoire Lagrange, Bd de l’Observatoire, CS 34229, 06304 Nice Cedex 4, France

<sup>8</sup> Italian National Agency for New Technologies, Energy and Sustainable Economic Development (ENEA), via Anguillarese 301, Rome, Italy

<sup>9</sup> Institut polaire français Paul Émile Victor and Programma Nazionale di Ricerche in Antartide, Concordia Station, Antarctica

<sup>10</sup> Istituto Nazionale di Astrofisica, Osservatorio Astronomico di Cagliari, Italy

<sup>11</sup> Department of Physics & Astronomy, University of Rochester, Rochester, NY 14627, USA

<sup>12</sup> Department of Physics, University of California at Santa Barbara, Santa Barbara, CA 93106, USA

<sup>13</sup> Department of Physics and Astronomy, Astronomy and Space Physics, Uppsala University, 751 20 Uppsala, Sweden

<sup>14</sup> Department of Physics, University of Oxford, Oxford OX1 3RH, UK

<sup>15</sup> Space Telescope Science Institute, 3700 San Martin Drive, Baltimore, MD 21218, USA

<sup>16</sup> Jet Propulsion Laboratory, California Institute of Technology, 4800 Oak Grove Drive, M/S321-100, Pasadena, CA 91109, USA

<sup>17</sup> LESIA, Observatoire de Paris, Université PSL, CNRS, Sorbonne Université, Université de Paris, 5 place Jules Janssen, 92195 Meudon, France

<sup>18</sup> Research School of Astronomy and Astrophysics, Australian National University, Canberra, ACT 2611, Australia

<sup>19</sup> South African Astronomical Observatory, Observatory Rd, Observatory Cape Town, 7700 Cape Town, South Africa

<sup>20</sup> Department of Astronomy, University of Cape Town, Rondebosch, 7700 Cape Town, South Africa

<sup>21</sup> Astronomy Department, University of California, Berkeley, CA 94720, USA

<sup>22</sup> SETI Institute, Carl Sagan Center, 189 Bernardo Ave., Mountain View CA 94043, USA

<sup>23</sup> Institute of Astrophysics, FORTH, GR-71110 Heraklion, Greece

<sup>24</sup> Center for Interdisciplinary Exploration and Research in Astrophysics (CIERA) and Department of Physics and Astronomy, Northwestern University, Evanston, IL 60208, USA

<sup>25</sup> Johns Hopkins APL, Laurel, MD, USA

<sup>26</sup> Johns Hopkins Applied Physics Laboratory, 11100 Johns Hopkins Road, Laurel, MD, 20723, USA

<sup>27</sup> School of Physical Sciences and Centre for Astrophysics & Relativity, Dublin City University, Glasnevin, Dublin 9, Ireland

<sup>28</sup> IPAG, Univ. Grenoble Alpes, CNRS, IPAG, 38000 Grenoble, France

<sup>29</sup> Univ. Grenoble Alpes, CNRS, IPAG, 38000 Grenoble, France

<sup>30</sup> European Southern Observatory, Karl-Schwarzschild-Straße 2, 85748 Garching, Germany

<sup>31</sup> Institute of Astronomy, Madingley Road, Cambridge CB3 0HA, UK

<sup>32</sup> Department of Physics, University of Warwick, Gibbet Hill Road, Coventry CV4 7AL, UK

<sup>33</sup> Centre for Exoplanets and Habitability, University of Warwick, Gibbet Hill Road, Coventry CV4 7AL, UK

<sup>34</sup> Shanghai Observatory, Chinese Academy of Sciences, PR China

<sup>35</sup> Purple Mountain Observatory, Chinese Academy of Science, Nanjing 210008, PR China

## Appendix A: TESS frequency analysis

### A.1. Frequency list

**Table A.1.** Pulsational frequencies, amplitudes in instrumental millimagnitudes, and normalized flux in parts per million, phases, and signal-to-noise ratio sorted by the pre-whitening sequence.

#	Freq. ( $d^{-1}$ )	Ampl. (mmag)	Ampl. (ppm)	Phase	S/N
1	47.43895(6)	1.029(9)	948(9)	0.9071(14)	20.6
2	53.69166(7)	0.948(9)	873(9)	0.2782(16)	19.4
3	50.49168(7)	0.926(9)	852(9)	0.5567(16)	23.4
4	54.23716(12)	0.553(9)	509(9)	0.982(3)	22.8
5	39.06315(15)	0.442(9)	407(9)	0.699(3)	22.5
6	46.54259(16)	0.415(9)	382(9)	0.391(4)	18.7
7	48.9192(3)	0.230(9)	212(9)	0.950(6)	17.3
8	43.5283(3)	0.214(9)	197(9)	0.029(7)	19.9
9	47.2853(4)	0.182(9)	168(9)	0.186(8)	16.2
10	57.4525(4)	0.164(9)	151(9)	0.577(9)	18.0
11	34.7605(5)	0.143(9)	131(9)	0.754(10)	23.7
12	38.1297(5)	0.131(9)	121(9)	0.980(11)	20.2
13	45.2698(5)	0.120(9)	110(9)	0.411(12)	12.8
14	51.4969(6)	0.118(9)	109(9)	0.397(13)	14.7
15	47.2686(7)	0.093(9)	85(9)	0.419(16)	12.3
16	50.8310(8)	0.086(9)	79(9)	0.630(17)	12.9
17	49.7131(8)	0.085(9)	78(9)	0.290(17)	11.3
18	53.8545(8)	0.085(9)	78(9)	0.566(17)	9.5
19	44.6833(8)	0.084(9)	77(9)	0.297(18)	11.3
20	65.1356(8)	0.083(9)	76(9)	0.350(18)	17.9
21	43.8292(8)	0.082(9)	76(9)	0.555(18)	16.3
22	49.5595(8)	0.079(9)	73(9)	0.980(19)	13.4
23	42.0365(9)	0.077(9)	71(9)	0.327(19)	11.1
24	54.2269(9)	0.073(9)	67(9)	0.51(2)	10.0
25	41.6498(9)	0.071(9)	65(9)	0.59(2)	13.0
26	48.1381(10)	0.064(9)	59(9)	0.23(2)	11.2
27	45.8998(10)	0.064(9)	59(9)	0.73(2)	12.4
28	50.2689(12)	0.054(9)	50(9)	0.90(3)	12.1
29	75.6780(13)	0.052(9)	48(9)	0.68(3)	12.2
30	58.3469(13)	0.050(9)	46(9)	0.61(3)	11.3
31	45.4375(14)	0.047(9)	44(9)	0.00(3)	12.3
32	54.4625(14)	0.047(9)	43(9)	0.16(3)	8.1
33	53.6827(15)	0.042(9)	39(9)	0.16(3)	7.3
34	53.5521(16)	0.040(9)	37(9)	0.48(4)	7.7
35	42.1735(16)	0.040(9)	37(9)	0.70(4)	9.5
36	58.2515(17)	0.039(9)	36(9)	0.81(4)	10.5
37	42.3963(17)	0.039(9)	36(9)	0.68(4)	11.5

### A.2. Gaussian high-pass filter

By applying a Gaussian high-pass filter on the TESS light curve (see Fig. A.1), the long-term variations such as systematics and the exocomets are significantly weakened. At the same time however, the higher frequencies related to the  $\delta$  Scuti pulsations are preserved.

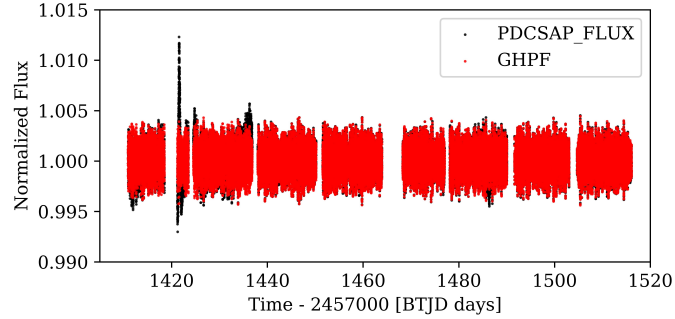


**Fig. A.1.** Comparison of the PDCSAP light curve (black in the background) and the Gaussian high-pass filter (red dots) of it. The Gaussian high-pass filter clearly shows less long-term variations in the light curve.